#### **PAPER**

# Uncertainty quantification and prediction for mechanical properties of graphene aerogels via Gaussian process metamodels

To cite this article: Bowen Zheng et al 2021 Nano Futures 5 045004

View the article online for updates and enhancements.

## You may also like

- lce-templated hybrid graphene oxide—graphene nanoplatelet lamellar architectures: tuning mechanical and electrical properties
   Pei Yang, Gustavo Tontini, Jiacheng Wang et al.
- Adsorption of tobacco-specific nitrosamine 4-(methylnitrosamino) -1- (3-pyridyl)-1butanone from aqueous solution with graphene aerogel T G Xu, R Shi, N Lu et al.
- <u>Supercritical fluids in chemistry</u> Evgenii S. Alekseev, Alexander Yu. Alentiev, Anastasia S. Belova et al.





RECEIVED

16 October 2021

REVISED 16 November 2021

ACCEPTED FOR PUBLICATION

22 November 2021

PUBLISHED

24 December 2021

#### **PAPER**

## Uncertainty quantification and prediction for mechanical properties of graphene aerogels via Gaussian process metamodels

Bowen Zheng<sup>1</sup>, Zeyu Zheng<sup>2</sup> and Grace X Gu<sup>1,\*</sup>

- Department of Mechanical Engineering, University of California, Berkeley, CA 94720, United States of America
- <sup>2</sup> Department of Industrial Engineering and Operations Research, University of California, Berkeley, CA 94720, United States of America
- \* Author to whom any correspondence should be addressed.

E-mail: ggu@berkeley.edu

**Keywords:** graphene aerogels, molecular dynamics, Gaussian process, nanomaterials, mechanical properties Supplementary material for this article is available online

#### **Abstract**

Graphene aerogels (GAs), a special class of 3D graphene assemblies, are well known for their exceptional combination of high strength, lightweightness, and high porosity. However, due to microstructural randomness, the mechanical properties of GAs are also highly stochastic, an issue that has been observed but insufficiently addressed. In this work, we develop Gaussian process metamodels to not only predict important mechanical properties of GAs but also quantify their uncertainties. Using the molecular dynamics simulation technique, GAs are assembled from randomly distributed graphene flakes and spherical inclusions, and are subsequently subject to a quasi-static uniaxial tensile load to deduce mechanical properties. Results show that given the same density, mechanical properties such as the Young's modulus and the ultimate tensile strength can vary substantially. Treating density, Young's modulus, and ultimate tensile strength as functions of the inclusion size, and using the simulated GA results as training data, we build Gaussian process metamodels that can efficiently predict the properties of unseen GAs. In addition, statistically valid confidence intervals centered around the predictions are established. This metamodel approach is particularly beneficial when the data acquisition requires expensive experiments or computation, which is the case for GA simulations. The present research quantifies the uncertain mechanical properties of GAs, which may shed light on the statistical analysis of novel nanomaterials of a broad variety.

#### 1. Introduction

Nanomaterials have influenced the energy and healthcare fields due to their unique optical, electronic, and mechanical properties [1–6]. For instance, graphene sheets are considered the strongest material ever tested due to their planar hexagonal lattice structure and the covalent bonding between carbon atoms and have been widely studied in the literature [7–10]. As a 3D extension of graphene, graphene aerogels (GAs), 3D porous assemblies of 2D graphene sheets, inherit many properties of graphene and manifest a desirable combination of low density and high strength [11, 12]. Notably, GAs with a density lower than that of air have been fabricated by assembling commercial carbon nanotubes and chemically converted graphene sheets [13], which may substitute for helium to infill unpowered flight balloons. In addition to being ultra-lightweight, GAs also possess other excellent material properties such as high specific surface area (due to high porosity) [14–16], high conductivity [17, 18], and good thermal stability [19]. As a result, GAs have quickly drawn research attention since their first fabrication, and have become an enticing candidate for various cutting-edge applications such as supercapacitors [20–22], gas sensing [15, 23], energy storage [24–26], oil sorption [27], among others.

For the mechanical properties of GAs, both experimental and computational studies have been conducted. Experimentally, Zhu *et al* conducted compression tests and measured the compressive stress–strain curves of 3D periodic GA microlattices [28]. Cheng *et al* showed that a 75.0 mg GA cylinder with a bulk density of 56.2 mg cm<sup>-3</sup> could support at least 26 000 times its own weight [29]. Zhang *et al* reported that GA–polydimethylsiloxane composites can sustain a compressive strain up to 80% and a tensile strain up to 90% [30]. Computationally, Qin *et al* conducted molecular dynamics (MD) simulations to study the mechanics of porous 3D graphene assemblies, and showed that the mechanical properties decrease with density faster than those of polymer foams [31]. Patil *et al* systematically investigated the fracture behavior [32] and the shock wave response [33] using MD simulations, and showed that GAs can be a promising material for shockwave and energy absorption applications.

Although recent studies on the mechanics of GAs have been fruitful, the observed high stochasticity of the mechanical properties of GAs remains unaddressed. For example, under a specific material density, GAs show a wide range of Young's modulus and tensile strength. This phenomenon is not particularly surprising, because the microstructures of GAs can be highly random and are difficult to control during the condensation process in both experiments and simulations. Nevertheless, previous studies either have not obtained enough data points under one density, or have largely grappled with this issue by averaging the test results. An understanding and quantitative modeling of the uncertainties in mechanical properties of GAs is crucial for the broader applications of GAs. In addition, MD simulations of GAs can be expensive, mostly because of the time-consuming assembling procedure, which consists of a number of annealing cycles (meanwhile the mechanical testing portion is relatively fast). Therefore, an interpolation method to predict properties of GAs that have not been simulated is much desired.

In this paper, we develop Gaussian process metamodels to not only predict important mechanical properties of GAs but also quantify their uncertainties. We first assemble and condense GAs via annealing cycles in the MD simulation, and subsequently subject GAs to a quasi-static uniaxial tensile load to deduce mechanical properties such as the Young's modulus and the ultimate tensile strength. A total of 270 GAs with a range of densities are simulated. Different from previous literature where the mechanical properties of GAs are treated as a function of the density, we consider the density, the Young's modulus and the ultimate tensile strength as functions of the size of the inclusions, which dictates the GA microstructure and thus mechanical properties in a complex fashion. Using the properties of the simulated GAs as the training data, we build Gaussian process metamodels that not only predict the properties of unseen GAs but also establish statistically valid confidence intervals centered around the predictions. This work quantifies the uncertain mechanical properties of GAs, which may shed light on the statistical analysis of novel nanomaterials of a broad variety.

#### 2. Methods

The starting point for GA fabrication in MD simulations comprises of 100 functional group-free square-shaped graphene flakes and 100 spherical inclusions, which mimic the effect of water clusters in freeze-casting porous graphene materials [34], as shown in figure 1(a). The side lengths of the graphene flakes L are sampled by a log-normal distribution to avoid negative values (illustrated in figure 1(b)), of which the probability density function is

$$p(L) = \frac{1}{L\sigma_L \sqrt{2\pi}} e^{-(\log L - \mu)^2 / 2\sigma_L^2}$$
 (1)

where

$$\sigma_L = \sqrt{\log\left(\frac{L_{\rm std}}{\bar{L}^2} + 1\right)} \tag{2}$$

and

$$\mu = \log \bar{L} - \frac{\sigma_L^2}{2} \tag{3}$$

are functions related to the mean value  $\bar{L}=12$  Å and the standard deviation  $L_{\rm std}=4.8$  Å [31]. The size of the spherical inclusions is constant, quantified by an effective radius  $R_{\rm eff}$ .  $R_{\rm eff}$  is given by  $R_{\rm eff}=2^{1/6}\sigma$ , where  $\sigma$ , the only simulation parameter that is variable in this study, encodes the equilibrium distance between two inclusions and between an inclusion and a carbon atom (see supplementary data for details (available online at stacks.iop.org/NANOF/5/045004/mmedia)). It has been shown in the published results that the density of

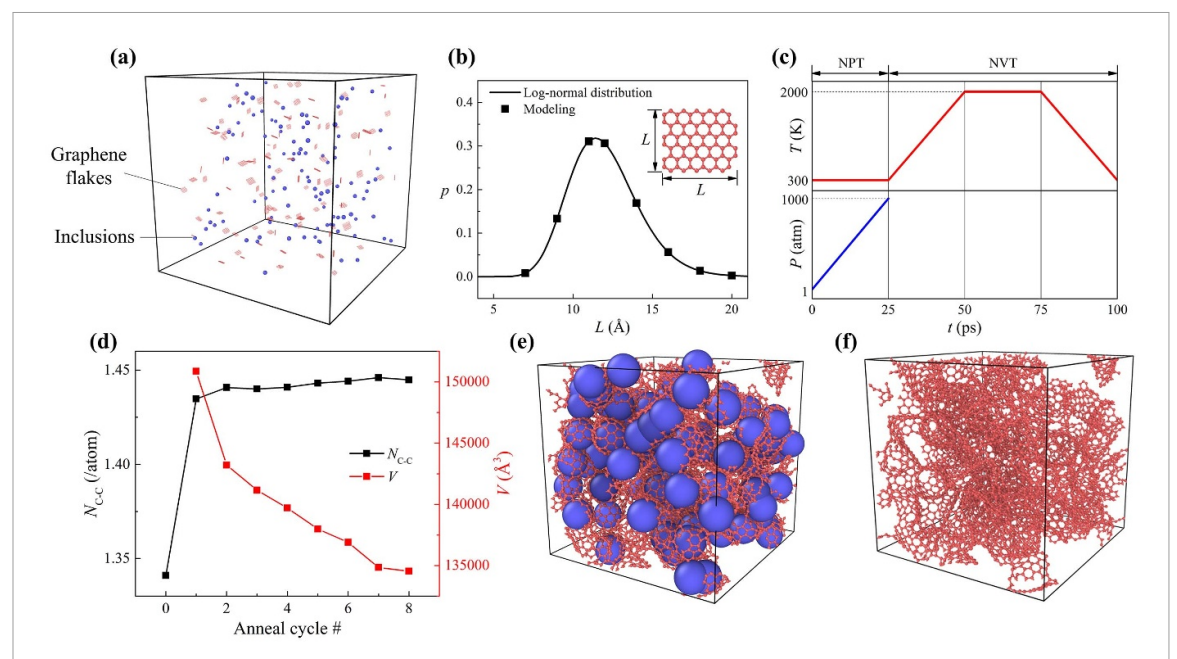


**Figure 1.** Construction of GAs in the MD simulation. (a) Initial stage of the material system. (b) Probability distribution of the graphene flake side length L. (c) Targeted temperature and pressure under NPT and NVT ensembles within one annealing cycle. (d) Number of C–C bonds per atom  $N_{C-C}$  and system volume V as functions of the annealing cycle number. (e) An example of material system configurations immediately after 8 annealing cycles. (f) Final configuration of a GA after spherical inclusions are removed.

GAs decreases as the spherical inclusions enlarge [31]. The spatial distributions of both graphene flakes and inclusions are uniformly random over a cubic simulation box. The orientations of graphene flakes are also random, dictated by the following 3D rotation tensor

$$R = R_z(\gamma) R_y(\beta) R_x(\alpha) = \begin{bmatrix} \cos \gamma & -\sin \gamma & 0 \\ \sin \gamma & \cos \gamma & 0 \\ 0 & 0 & 1 \end{bmatrix} \begin{bmatrix} \cos \beta & 0 & \sin \beta \\ 0 & 1 & 0 \\ -\sin \beta & 0 & \cos \beta \end{bmatrix} \begin{bmatrix} 1 & 0 & 0 \\ 0 & \cos \alpha & -\sin \alpha \\ 0 & \sin \alpha & \cos \alpha \end{bmatrix}$$
(4)

where  $\gamma$ ,  $\beta$ , and  $\alpha$  are independently and identically distributed from 0 to  $\pi$ . The initial density of the material system is 2 mg cm<sup>-3</sup>, and the initial volume of the simulation box is  $6.80 \times 10^7$  Å<sup>3</sup>. These graphene flakes are subsequently fused into a 3D GA structure. MD simulations are performed using the open-source program Large-scale Atomic/Molecular Massively Parallel Simulator (LAMMPS) [35] and the Extreme Science and Engineering Discovery Environment (XSEDE) computing resources. All MD simulation details are summarized in the supplementary data.

The condensation of the material system is realized by a number of designed annealing cycles. Each cycle consists of four stages: (a) in the isothermal-isobaric (NPT) ensemble where the temperature is maintained at  $T = 300 \,\mathrm{K}$  and the pressure P increases linearly from 1 atm to 1000 atm; (b) in the canonical (NVT) ensemble where the temperature T increases linearly from 300 K to 2000 K; (c) in the NVT ensemble where the temperature is held at  $T = 2000 \,\mathrm{K}$ ; (d) in the NVT ensemble where the temperature T decreases linearly from 2000 K to 300 K. The duration of each stage is 25 ps. The setting of one entire annealing cycle is illustrated in figure 1(c), and the true recorded temperature and pressure in multiple cycles are shown in figure S1. All volume change takes place in the first stage where the system volume is uncontrolled, while in the subsequent three stages, the system volume remains constant. The system volume V as a function of experienced annealing cycle number is shown in figure 1(d). As the annealing cycles go on, the system volume decreases, suggesting the material is condensed during the process. During annealing cycles, new C-C bonds are formed across initially disconnected graphene flakes. The number of C-C bonds per atom  $N_{\rm C-C}$  is used to quantify the structural integrity of the GAs. After eight annealing cycles,  $N_{\rm C-C}$  converges to 1.45, close to the value 1.5 for an infinitely large graphene sheet, as is shown in figure 1(d). This suggests that initially disconnected graphene flakes are now well integrated and will only improve marginally as more annealing cycles are simulated. Hence, and for the sake of efficiency, all GAs in this study are prepared with eight annealing cycles. An example of the closely packed GA structure and spherical inclusions after eight annealing cycles is shown in figure 1(e). Next, the inclusions are deleted from the system, and the 3D GA is relaxed in the NVT ensemble at  $T = 300 \,\mathrm{K}$  for another 25 ps to produce the final GA structure, as illustrated in figure 1(f). The final GA, with a density of 0.986 g cm<sup>-3</sup>, is structurally stable.

B Zheng et al

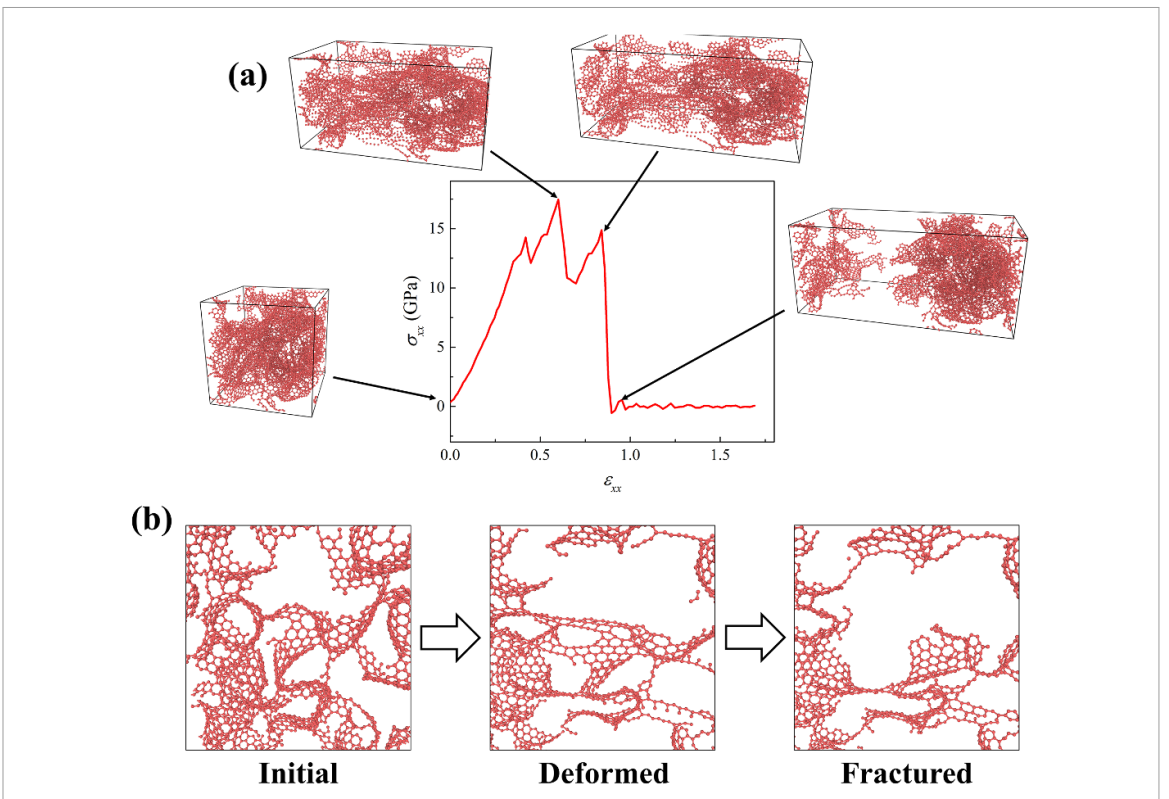


**Figure 2.** Stress–strain curve and deformation/fracture modes of one example GA. (a) Stress–strain curve of the GA under a uniaxial tensile load.  $\sigma_{xx}$  and  $\varepsilon_{xx}$  denote the stress and the strain in the loading direction. GA molecular configurations at critical points on the stress–strain curve are provided. The density of the GA in this example is 0.924 g cm<sup>-3</sup>. (b) Illustrations of local deformation and fracture modes of the GA.

For the mechanical testing, a uniaxial tensile load is applied to the prepared GAs in a quasi-static, incremental manner. At each step, the simulation box is deformed for a 1% uniaxial strain in x direction in the NPT ensemble with  $T = 300 \,\mathrm{K}$  and P = 1 atm applied to the two unloaded y and z directions. Each strain increment is followed by an energy minimization and equilibration in the NVT ensemble with  $T = 300 \,\mathrm{K}$ . An example stress-strain curve, along with GA shapes corresponding to several critical points on the curve, are shown in figure 2. The stress-strain curve exhibits a clearly defined linear part, followed by multiple peaks and a catastrophic failure. This suggests that the GA undergoes a progressive failure upon uniaxial tensile loading. The failure strain is close to 0.9, consistent with the result in [30], and is much enhanced compared to that of 2D graphene sheets (0.2–0.3). However, the Young's modulus (29.5 GPa) and the ultimate tensile stress (17.5 GPa) are much reduced compared to the defect-free graphene sheets (with a Young's modulus of 1000 GPa and an ultimate tensile strength of 130 GPa [7]). Different from anisotropic 2D graphene sheets, GAs are in principle isotropic due to the assembly of a large amount of randomly distributed graphene flakes. Therefore, we use the Young's modulus and the tensile strength in the loading direction to represent the Young's modulus and the tensile strength of the GA material. The stress–strain curve of one GA subject to cyclic loading is provided in figure S3, where the first cycle exhibits some elastic hysteresis while the subsequent cycles do not.

## 3. Results and discussion

To investigate the stochastic nature of GA mechanical properties, a total of 270 GAs are simulated. Nine values of  $\sigma \in [2,3,\dots,10]$  Å (equivalent to  $R_{\rm eff} \in 2^{1/6}$   $[2,3,\dots,10]$  Å) are used to generate GA structures, where each  $\sigma$  (or  $R_{\rm eff}$ ) value generates 30 random configurations. GA density  $\rho$  as a function of  $R_{\rm eff}$  is illustrated in figure S2. It is shown that  $\rho$  decreases as  $R_{\rm eff}$  increases, in good agreement with previously reported results [31]. To investigate the statistics of the bond breaking behavior of GAs, the fractions of broken bonds of the GA model where  $R_{\rm eff} = 2^{1/6} \times 5$  Å = 4.45 Å are computed based on 30 data points. The mean and the standard deviation of the fraction is 0.39% and 0.23%, suggesting that the catastrophic failure of GAs is related to a small number of broken bonds at critical locations. The histogram of the fraction of broken bonds is provided in figure S4. Figure 3 shows scatter plots of the Young's modulus E and the ultimate tensile stress  $\sigma_{\rm u}$  against  $\rho$  for all 270 GAs, where both E and  $\sigma_{\rm u}$  increase as  $\rho$  increases. In addition, the

B Zheng et al

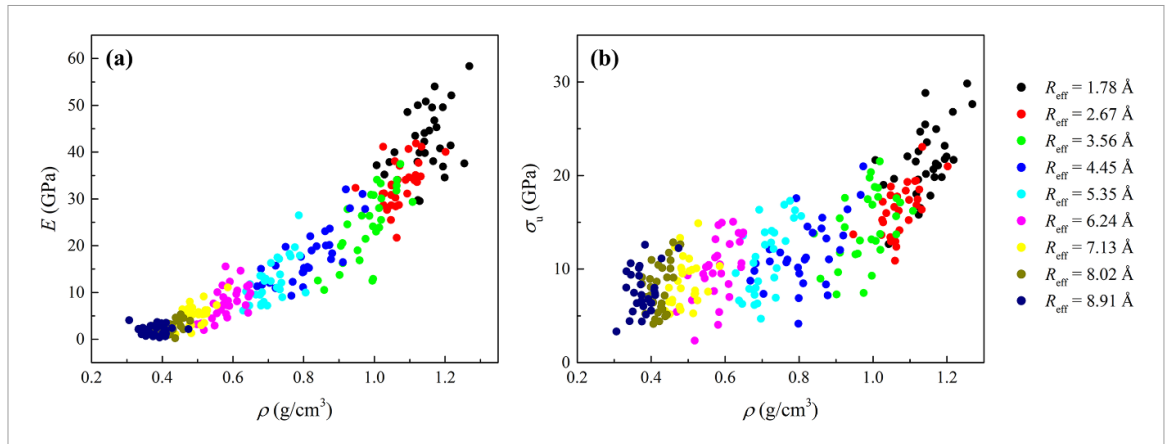
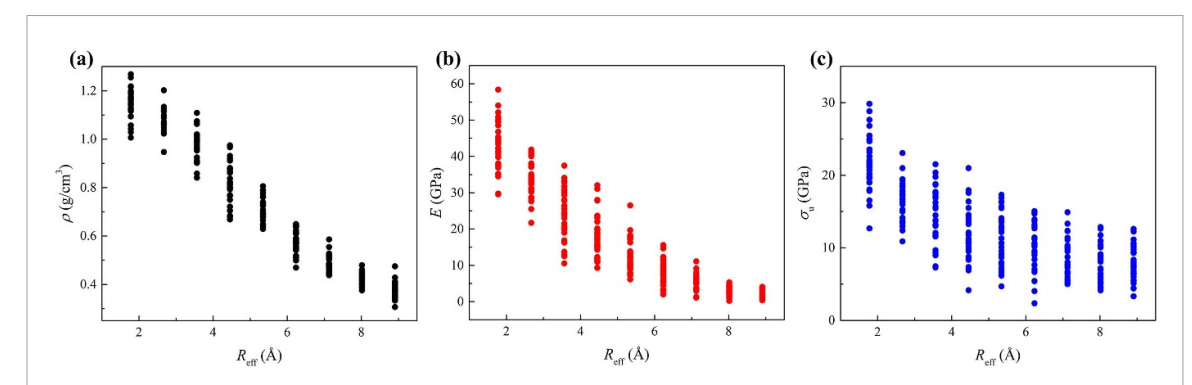


Figure 3. Scatter plots of the Young's modulus and the ultimate stress against the density of all 270 GAs. Plots of (a) the Young's modulus and (b) the ultimate tensile stress.



**Figure 4.** Scatter plots of the GA density, Young's modulus, and ultimate tensile stress against the effective radius of the inclusions. Plots of (a) the density, (b) the Young's modulus, and (c) the ultimate tensile stress.

variation E is relatively small for small  $\rho$ , but increases as  $\rho$  increases. However, the variation of  $\sigma_{\rm u}$  is comparatively larger and independent of  $\rho$ . This shows that the randomness of the GA microstructure has different influencing mechanisms on the stiffness and the strength. One hypothesis is that the strength of GAs is more responsive to the progressive failure mode, which is rather unrelated to the density but highly dependent on the microstructure. The results are further clustered by  $R_{\rm eff}$ , where the data points originating from different  $R_{\rm eff}$  are colored differently. It is observed that between clusters there is significant overlapping in both horizontal and vertical directions, indicating that both density and mechanical properties are random given one  $R_{\rm eff}$  value. Even though some data points on figure 3(b) have achieved roughly 25 times as strong as mild steel with a density 10% that of mild steel, this observed randomness poses substantial difficulty and uncertainty for engineers to effectively design and use GAs.

Previous works in literature treat mechanical properties of GAs, such as the Young's modulus and the ultimate tensile strength, as functions of the density [31, 32], just like in figure 3. However, in our simulations the density is not a variable that we have full control over, and the mechanical properties can vary widely given one specific density value. Instead, we consider the density  $\rho$ , Young's modulus E, and ultimate tensile strength  $\sigma_{\rm u}$  as functions of  $R_{\rm eff}$ , the only parameter in this study that dictates the GA microstructure and, thus, mechanical properties. To this end, we plot  $\rho$ , E, and  $\sigma_{\rm u}$  against  $R_{\rm eff}$ , as shown in figure 4. Now the results are transformed from nine heavily overlapped clusters to 1D distributions at nine different locations. This allows us to fit the properties under each  $R_{\rm eff}$  to a statistical distribution such as the Gaussian distribution, which establishes confidence intervals. More importantly, this presentation of the data offers an opportunity to interpolate and predict properties of unsurveyed  $R_{\rm eff}$  given noise. This is particularly valuable in that the MD simulations of GA are rather computationally expensive and simulating GAs given more densely distributed  $R_{\rm eff}$  are very time-consuming.

Here, we propose a metamodel approach that employs a non-parametric regression method called Gaussian process regression (GPR), a probabilistic interpolation approach that integrates observed samples and prior distribution and covariances [36, 37]. In recent years, GPR has been widely applied in materials design and discovery problems [38, 39]. GPR predicts the value of a function at a target point by computing a weighted average of the known values of the function (the training data) in a statistically principled way.

Nano Futures 5 (2021) 045004 B Zheng et al

The weights are determined by a covariance function (or a kernel) that specifies the covariance between pairs of random variables. Concretely, given a training set  $\mathcal{D} = \{(\mathbf{x}_i, y_i) | i = 1, ..., n\}$ , where  $\mathbf{x}_i$  denotes an input vector of a dimension D and  $y_i$  denotes a scalar output, a noise-free covariance function can be written as

$$cov(y_p, y_q) = cov(f(\mathbf{x}_p), f(\mathbf{x}_q)) = k(\mathbf{x}_p, \mathbf{x}_q)$$
(5)

where  $k(\cdot, \cdot)$  denotes a kernel function, or in matrix form

$$cov(\mathbf{y}) = K(X, X) \tag{6}$$

where **y** is an output vector; X is a  $D \times n$  design matrix aggregated by n input vectors; K is an  $n \times n$  kernel matrix. In this study, we use the linear combination of two radial-basis functions as the covariance function, given by

$$k\left(\mathbf{x}_{p}, \mathbf{x}_{q}\right) = s_{1}^{2} \exp\left(-\frac{\mathbf{x}_{p} - \mathbf{x}_{q_{2}}^{2}}{2l_{1}^{2}}\right) + s_{2}^{2} \exp\left(-\frac{\mathbf{x}_{p} - \mathbf{x}_{q_{2}}^{2}}{2l_{2}^{2}}\right)$$
(7)

where  $s_1^2$  and  $s_2^2$  are scaling parameters known as the process variances;  $l_1^2$  and  $l_2^2$  are length-scale parameters;  $\| \cdot \|$  denotes the  $L^2$  norm. From the expression, the covariance between two data points depends only on their Euclidean distance and not on their absolute values. For noisy cases (as is fit to describe the simulation results in this study), the kernel matrix K is regularized by the 'nugget', a positive value  $\tau_i^2$  ( $i=1,\ldots,n$ ) added to the main diagonal of K. This corresponds to a probabilistic model with an additive white noise of variance  $\tau_i^2$  below

$$y_i = f(\mathbf{x}_i) + \varepsilon_i \tag{8}$$

where  $\varepsilon_i \sim \mathcal{N}\left(0, \tau_i^2\right)$ . Here, we use the shorthand representation of a probability distribution, where  $\mathcal{N}\left(\mu, \sigma^2\right)$  denotes a normal distribution,  $\mathcal{N}$ , with mean,  $\mu$ , and variance,  $\sigma^2$ . The covariance function now becomes

$$cov(y_p, y_q) = k(\mathbf{x}_p, \mathbf{x}_q) + \tau_p^2 \delta_{pq}$$
(9)

where  $\delta_{pq}$  is the Kronecker delta which equals 1 if p = q and 0 otherwise, or in matrix form

$$cov(\mathbf{y}) = K(X, X) + \Lambda I \tag{10}$$

where  $\Lambda = \operatorname{diag}\left(\tau_1^2, \tau_2^2, \dots, \tau_n^2\right)$  and I is the  $n \times n$  identity matrix. The 'nugget' regularization improves the condition number of the covariance matrix by increasing the eigenvalues by  $\tau_i^2$ . Additionally, it causes the GPR to smoothen the data and become non-interpolating. In this study,  $\tau_i^2$  takes on the variance of the training data under each  $R_{\text{eff}}$ . The parameters of the covariance function in equation (9) are optimized during fitting by maximizing the log marginal likelihood below

$$\log p(\mathbf{y}|X) = -\frac{1}{2}\mathbf{y}^{\mathrm{T}}(K + \Lambda I)^{-1}\mathbf{y} - \frac{1}{2}\log|K + \Lambda I| - \frac{n}{2}\log 2\pi.$$
 (11)

To obtain predictions at an unseen point of interest  $\mathbf{x}_*$ , the predictive distribution can be calculated by weighting all possible predictions by their calculated posterior distribution as follows

$$p(f_*|\mathbf{x}_*, X, \mathbf{y}) = \int p(f_*|\mathbf{x}_*, \mathbf{w}) p(\mathbf{w}|X, \mathbf{y}) d\mathbf{w}$$
(12)

where  $f_*$  is the predicted function value at target  $\mathbf{x}_*$ , and  $\mathbf{w}$  is the weight vector. For GPR, the joint distribution of the training data and the function values at the locations of interest under the prior can be written as

$$\begin{bmatrix} \mathbf{y} \\ \mathbf{f}_* \end{bmatrix} \sim \mathcal{N} \left( \mathbf{0}, \begin{bmatrix} K(X,X) + \Lambda I & K(X,X_*) \\ K(X_*,X) & K(X_*,X_*) \end{bmatrix} \right)$$
(13)

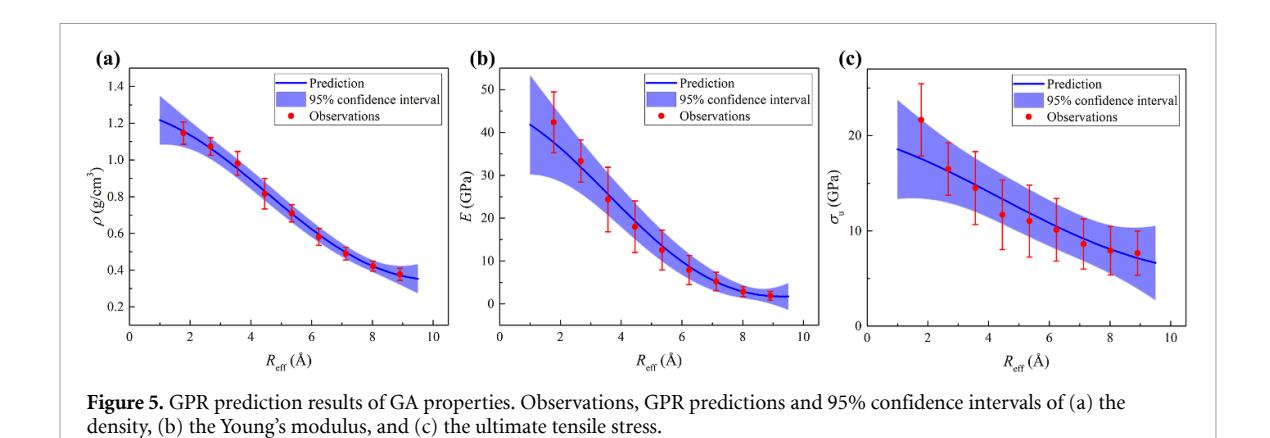
where  $\mathbf{f}_*$  is the predicted function vector at target design matrix  $X_*$ . We reach the key predictive equations for GPR

$$\mathbf{f}_*|X_*, X, \mathbf{y} \sim \mathcal{N}\left(\bar{\mathbf{f}}_*, \operatorname{cov}(\mathbf{f}_*)\right)$$
 (14)

where

$$\bar{\mathbf{f}}_* \triangleq \mathbb{E}\left[\mathbf{f}_* | X_*, X, \mathbf{y}\right] = K(X_*, X) \left(K(X, X) + \Lambda I\right)^{-1} \mathbf{y} \tag{15}$$

B Zheng et al



is the mean of the predicted function vectors, which is considered as the GPR prediction, and

$$cov(\mathbf{f}_*) = K(X_*, X_*) - K(X_*, X)(K(X, X) + \Lambda I)^{-1}K(X, X_*)$$
(16)

is the predicted covariance matrix. The vector of the predicted variance  $\sigma_*^2$  can be obtained from the diagonal of  $\text{cov}(\mathbf{f}_*)$ 

$$\sigma_*^2 = \operatorname{diag}(\operatorname{cov}(\mathbf{f}_*)). \tag{17}$$

Finally, the 95% confidence interval can then be established as  $[\mathbf{f}_* - 1.96\boldsymbol{\sigma}_*, \bar{\mathbf{f}}_* + 1.96\boldsymbol{\sigma}_*]$ . The GPR results of the present study are shown in figure 5, where the GPR predicted means are plotted in solid lines and 95% confidence intervals are illustrated in shaded areas. Red dots and error bars are results from figure 4 that are used as the training data. The significance of this result is that given an  $R_{\rm eff}$  value, we are able to predict the most probable  $\rho$ , E, and  $\sigma_u$  of the unsimulated GA. Inversely, given target  $\rho$ , E, and  $\sigma_u$ , we know the  $R_{\text{eff}}$  value that gives us the best chance to achieve the goal. It is observed in figure 5 that we are more confident about  $\rho$ compared to E and  $\sigma_u$ . This is expected because  $R_{\text{eff}}$  intuitively has a more direct impact on the structural properties than on the mechanical properties. The causal inference between  $R_{\text{eff}}$ ,  $\rho$ , E, and  $\sigma_{\text{u}}$  will be studied in future work. In addition, for all three properties, the 95% confidence intervals are tighter in the middle compared to both ends. This observation indicates that there are more uncertainties if the GPR approach is used to do extrapolations compared to interpolations. We note that this is common in all metamodel approaches, because intrinsically there are more 'informative' data points available to do interpolations compared to extrapolations. From a quantitative perspective, the kernel becomes small fast (in this study, exponentially) as the target is farther away from the known data points, as indicated by equation (7). One can change the kernel to take different forms in practice, and they all will present a decaying phenomenon as the target is farther away. The difference would be how fast the kernel decays. Our recommendation is that, one can still use GPR to make predictions for extrapolations that are not too far away from the center of the data, but one should be aware of the level of uncertainties.

## 4. Conclusion

We constructed a bottom-up atomistic simulation model and a statistical metamodel to investigate the uncertain mechanical properties of GAs. Using MD simulations, GAs are firstly assembled from randomly distributed graphene flakes and spherical inclusions via annealing cycles, and are subsequently subject to a quasi-static uniaxial tensile load to deduce mechanical properties. Our results show that given a specific density, the Young's modulus and the ultimate tensile strength of GAs can vary substantially. Different from most previous literature where the mechanical properties of GAs are treated as a function of the density, we consider the density, the Young's modulus and the ultimate tensile strength as functions of the size of the inclusions, which dictates the GA microstructure and thus mechanical properties in a complex fashion. Using the properties of the simulated GAs as the training data, we build Gaussian process metamodels that not only predict the properties of unseen GAs but also establish statistically valid confidence intervals centered around the predictions. This metamodel approach is particularly beneficial when the data acquisition requires expensive experiments or computation, which is the case for the GA simulations. The present research quantifies the uncertain mechanical properties of GAs, which may shed light on the statistical analysis of novel nanomaterials of a broad variety. The causal modeling between the inclusion size, the density, and the mechanical properties of GAs will be conducted in future work.

### Data availability statement

All data that support the findings of this study are included within the article (and any supplementary files).

## Acknowledgments

This work used the Extreme Science and Engineering Discovery Environment (XSEDE) Bridges system, which is supported by National Science Foundation Grant Number ACI-1548562. The authors also acknowledge support from National Science Foundation Grant Number CMMI-2119276 and an NVIDIA GPU Seed Grant.

#### **ORCID iD**

Grace X Gu https://orcid.org/0000-0001-7118-3228

#### References

- [1] Roduner E 2006 Size matters: why nanomaterials are different Chem. Soc. Rev. 35 583-92
- [2] Pirzada M and Altintas Z 2019 Nanomaterials for healthcare biosensing applications Sensors 19 5311
- [3] Chen C-T, Chrzan D C and Gu G X 2020 Nano-topology optimization for materials design with atom-by-atom control *Nat. Commun.* 11 1–9
- [4] Zheng B and Gu G X 2020 Machine learning-based detection of graphene defects with atomic precision Nano-Micro Lett. 12 1-13
- [5] Guo Z and Tan L 2009 Fundamentals and Applications of Nanomaterials (Norwood, MA: Artech House)
- [6] Chen C-T, Martin-Martinez F J, Ling S, Qin Z and Buehler M J 2017 Nacre-inspired design of graphene oxide–polydopamine nanocomposites for enhanced mechanical properties and multi-functionalities Nano Futures 1 011003
- [7] Lee C, Wei X, Kysar J W and Hone J 2008 Measurement of the elastic properties and intrinsic strength of monolayer graphene Science 321 385–8
- [8] Zheng B, Zheng Z and Gu G X 2021 Scalable graphene defect prediction using transferable learning Nanomaterials 11 2341
- [9] Geim A K 2009 Graphene: status and prospects Science 324 1530-4
- [10] Zheng B and Gu G X 2019 Tuning the graphene mechanical anisotropy via defect engineering Carbon 155 697-705
- [11] Gorgolis G and Galiotis C 2017 Graphene aerogels: a review 2D Mater. 4 032001
- [12] Fang Q, Shen Y and Chen B 2015 Synthesis, decoration and properties of three-dimensional graphene-based macrostructures: a review *Chem. Eng. J.* 264 753–71
- [13] Sun H, Xu Z and Gao C 2013 Multifunctional, ultra-flyweight, synergistically assembled carbon aerogels Adv. Mater. 25 2554–60
- [14] Sui Z-Y, Meng Q-H, Li J-T, Zhu J-H, Cui Y and Han B-H 2014 High surface area porous carbons produced by steam activation of graphene aerogels *J. Mater. Chem.* A 2 9891–8
- [15] Long H, Harley-Trochimczyk A, Pham T, Tang Z, Shi T, Zettl A, Carraro C, Worsley M A and Maboudian R 2016 High surface area MoS<sub>2</sub>/graphene hybrid aerogel for ultrasensitive NO<sub>2</sub> detection Adv. Funct. Mater. 26 5158–65
- [16] Zhang E, Liu W, Liang Q, Liu X, Zhao Z and Yang Y 2019 Polypyrrole nanospheres@graphene aerogel with high specific surface area, compressibility, and proper water wettability prepared in dimethylformamide-dependent environment *Polymer* 185 121974
- [17] Worsley M A, Pauzauskie P J, Olson T Y, Biener J, Satcher J H and Baumann T F 2010 Synthesis of graphene aerogel with high electrical conductivity *J. Am. Chem. Soc.* 132 14067–9
- [18] Zhang X, Sui Z, Xu B, Yue S, Luo Y, Zhan W and Liu B 2011 Mechanically strong and highly conductive graphene aerogel and its use as electrodes for electrochemical power sources *J. Mater. Chem.* 21 6494–7
- [19] Li Z, Liu Z, Sun H and Gao C 2015 Superstructured assembly of nanocarbons: fullerenes, nanotubes, and graphene *Chem. Rev.* 115 7046–117
- [20] Yu Z, McInnis M, Calderon J, Seal S, Zhai L and Thomas J 2015 Functionalized graphene aerogel composites for high-performance asymmetric supercapacitors Nano Energy 11 611–20
- [21] Liu R, Wan L, Liu S, Pan L, Wu D and Zhao D 2015 An interface-induced Co-assembly approach towards ordered mesoporous carbon/graphene aerogel for high-performance supercapacitors *Adv. Funct. Mater.* 25 526–33
- [22] Yang Y, Xi Y, Li J, Wei G, Klyui N I and Han W 2017 Flexible supercapacitors based on polyaniline arrays coated graphene aerogel electrodes Nanoscale Res. Lett. 12 394
- [23] Liu X, Cui J, Sun J and Zhang X 2014 3D graphene aerogel-supported SnO<sub>2</sub> nanoparticles for efficient detection of NO<sub>2</sub> RSC Adv. 4 22601–5
- [24] Yang J, Zhang E, Li X, Zhang Y, Qu J and Yu -Z-Z 2016 Cellulose/graphene aerogel supported phase change composites with high thermal conductivity and good shape stability for thermal energy storage *Carbon* 98 50–57
- [25] Xia W et al 2017 High-performance energy storage and conversion materials derived from a single metal—organic framework/graphene aerogel composite Nano Lett. 17 2788–95
- [26] Kashyap S, Kabra S and Kandasubramanian B 2020 Graphene aerogel-based phase changing composites for thermal energy storage systems *J. Mater. Sci.* 55 4127–56
- [27] Hu H, Zhao Z, Gogotsi Y and Qiu J 2014 Compressible carbon nanotube–graphene hybrid aerogels with superhydrophobicity and superoleophilicity for oil sorption *Environ. Sci. Technol. Lett.* 1 214–20
- [28] Zhu C, Han T Y-J, Duoss E B, Golobic A M, Kuntz J D, Spadaccini C M and Worsley M A 2015 Highly compressible 3D periodic graphene aerogel microlattices Nat. Commun. 6 6962
- [29] Cheng Y, Zhou S, Hu P, Zhao G, Li Y, Zhang X and Han W 2017 Enhanced mechanical, thermal, and electric properties of graphene aerogels via supercritical ethanol drying and high-temperature thermal reduction *Sci. Rep.* 7 1439
- [30] Zhang Q, Xu X, Li H, Xiong G, Hu H and Fisher T S 2015 Mechanically robust honeycomb graphene aerogel multifunctional polymer composites Carbon 93 659–70

- [31] Qin Z, Jung G S, Kang M J and Buehler M J 2017 The mechanics and design of a lightweight three-dimensional graphene assembly Sci. Adv. 3 e1601536
- [32] Patil S P, Shendye P and Markert B 2020 Molecular investigation of mechanical properties and fracture behavior of graphene aerogel *J. Phys. Chem.* B 124 6132–9
- [33] Patil S P, Kulkarni A and Markert B 2021 Shockwave response of graphene aerogels: an all-atom simulation study *Comput. Mater. Sci.* 189 110252
- [34] Xie X, Zhou Y, Bi H, Yin K, Wan S and Sun L 2013 Large-range control of the microstructures and properties of three-dimensional porous graphene Sci. Rep. 3 2117
- [35] Plimpton S 1995 Fast parallel algorithms for short-range molecular dynamics J. Comput. Phys. 117 1–19
- [36] Ankenman B, Nelson B L and Staum J 2008 Stochastic kriging for simulation metamodeling 2008 Winter Simulation Conf. pp 362–70
- [37] Rasmussen C E 2004 Advanced Lectures on Machine Learning (ML Summer Schools 2003, Canberra, Australia, February 2–14, 2003, Tübingen, Germany, August 4–16, 2003, Revised Lectures) ed O Bousquet et al (Berlin: Springer) pp 63–71
- [38] Deringer V L, Bartók A P, Bernstein N, Wilkins D M, Ceriotti M and Csányi G 2021 Gaussian process regression for materials and molecules *Chem. Rev.* 121 10073–141
- [39] Noack M M, Doerk G S, Li R, Streit J K, Vaia R A, Yager K G and Fukuto M 2020 Autonomous materials discovery driven by Gaussian process regression with inhomogeneous measurement noise and anisotropic kernels *Sci. Rep.* 10 17663